

Adaptive resolvent analysis with application to high-enthalpy flows

By S. Gomez,[†] C. Williams, M. Di Renzo,[¶] P. Schmid^{||} AND B. McKeon[†]

A method is presented to efficiently and adaptively identify the regions in spectral space with the largest resolvent gain, termed adaptive resolvent analysis. At each iteration, sampled measurements of the resolvent gain and its gradients are used with Gaussian process regression (GPR) to build a surrogate surface with uncertainty in wavenumber space. The next wavenumbers to sample are determined by maximizing an acquisition function that balances exploitation and exploration. This method is applied to two different high-enthalpy flows—a turbulent boundary layer in thermochemical equilibrium with constant and varying specific gas constants, and a laminar boundary layer in chemical nonequilibrium. Resolvent analysis of these flows gives insight into the linear amplification mechanisms and coherent structures, along with a prediction of the length and timescales most influenced by changes in the transport properties via departures from the calorically perfect gas (CPG) assumption.

1. Introduction

Resolvent analysis is an equation-based modal analysis technique that is an attractive tool for flow modeling and flow control. The resolvent operator is equivalent to a linear transfer function that maps the forcing, the nonlinear terms in the equations or control inputs, to the associated output responses in a scale-dependent fashion through a Fourier transform in time and any homogeneous spatial directions. The Schmidt decomposition, or singular value decomposition (SVD) for discretized systems, of the resolvent operator identifies two orthonormal bases, one basis that identifies the optimal forcing modes and another basis containing the subsequent response modes. These two sets of bases are ranked by their singular values, the linear gain of the transfer function with respect to a chosen inner product. In spectral space for incompressible channel flows, the regions with high turbulent kinetic energy content overlap with regions where the resolvent operator is low rank (Moarref *et al.* 2013). For compressible wall-bounded flows, the linear amplification reveals a distinct delineation in spectral space between relatively supersonic and subsonic modes (Bae *et al.* 2020; Madhusudanan & McKeon 2022).

Although resolvent analysis relies on well-established linear algebra techniques, the required calculations can be expensive for all but the simplest geometries. Creating the resolvent operator and taking its SVD are both $\mathcal{O}(N^3)$ operations, where N is the number of state variables times the number of grid points. The number of state variables is large for nonparallel flows because multiple spatial dimensions need to be resolved. For chemically reacting flows, N increases due to the multiple species in mixture. For cases like these, where N is large, performing parameter sweeps is computationally expensive.

A method is presented that identifies and samples the regions of parameter space that

[†] California Institute of Technology

[¶] Centre Européen de Recherche et de Formation Avancée en Calcul Scientifique, France

^{||} King Abdullah University of Science and Technology, Saudi Arabia

lead to the largest resolvent gain, here termed adaptive resolvent analysis in the sense that the scheme updates with each new measurement by improving the surrogate surface. The method is based on Bayesian optimization, where all sampled measurements are used to create a model m with uncertainty s through GPR. The next points to sample are chosen by maximizing an acquisition function f_{ac} that depends on m and s in a way that balances exploration and exploitation. Exploration means that the method will sample regions with large uncertainty s , while exploitation will sample regions with the largest values predicted by the model m . Given a few initial samples, each subsequent iteration improves and updates m , while also sampling the regions in spectral space with the largest resolvent gain. Compared with a fixed grid parameter sweep, this method utilizes fewer query points while clustering the samples in the most energetic regions of the parameter space.

In Section 2, resolvent analysis is briefly described and the adaptive resolvent analysis algorithm is presented. The governing equations, inner products, and mean flow fields are then briefly discussed for a calorically imperfect ideal gas (CIG) and a mixture of ideal gases in chemical nonequilibrium. Section 3 demonstrates how adaptive resolvent analysis is able to sample the most energetic regions of parameter space, illuminating how varying transport properties affect the mechanisms for amplification. Finally, conclusions are drawn in Section 4.

2. Formulation and computational setup

2.1. Resolvent analysis

Consider a statistically stationary dynamical system with state $\tilde{\mathbf{q}} = \bar{\mathbf{q}} + \mathbf{q}$, where $\bar{\mathbf{q}}$ represents the steady mean field and \mathbf{q} is the fluctuation, evolving under a sufficiently smooth nonlinear differential operator, \mathbf{F} , with boundary conditions embedded such that

$$\frac{\partial \tilde{\mathbf{q}}}{\partial t} + \mathbf{F}(\tilde{\mathbf{q}}) = \mathbf{0}, \tilde{\mathbf{q}}(t=0) = \tilde{\mathbf{q}}_0. \quad (2.1)$$

The dynamical system can be rewritten as

$$\frac{\partial \mathbf{q}}{\partial t} + \mathbf{L}\mathbf{q} = -(\mathbf{F}(\tilde{\mathbf{q}}) - \mathbf{L}\mathbf{q}) \doteq \mathbf{n}, \quad (2.2)$$

where \mathbf{L} denotes the Jacobian of \mathbf{F} evaluated at $\bar{\mathbf{q}}$ and \mathbf{n} has a physical interpretation as the nonlinear terms in the governing equations. This decomposition depends on the choice of $\bar{\mathbf{q}}$, not necessarily a realizable state of the system. For a statistically stationary parallel flow, we take \mathbf{q} and \mathbf{n} as normal modes such that $[\mathbf{q}, \mathbf{n}] = [\hat{\mathbf{q}}, \hat{\mathbf{n}}](y) \exp(-i\omega t + k_x x + k_z z)$, where ω , k_x , and k_z are the temporal frequency, streamwise wavenumber, and spanwise wavenumber, respectively. Equation (2.2) then becomes

$$\left(-i\omega\mathbf{I} + \hat{\mathbf{L}}\right) \hat{\mathbf{q}} = \hat{\mathbf{n}}. \quad (2.3)$$

In what follows, $\hat{\mathbf{n}}$ will be an arbitrary input \mathbf{f} independent of the nonlinear form. To ensure that $(-i\omega\mathbf{I} + \hat{\mathbf{L}})$ is invertible, ω is chosen to not be an eigenvalue of $\hat{\mathbf{L}}$. The response $\hat{\mathbf{q}}$ is governed by

$$\hat{\mathbf{q}} = \left(-i\omega\mathbf{I} + \hat{\mathbf{L}}\right)^{-1} \mathbf{f} = \mathbf{H}\mathbf{f}, \quad (2.4)$$

where \mathbf{H} is the resolvent operator. The relevant inner products are defined as

$$\langle \mathbf{f}_1, \mathbf{f}_2 \rangle_f = \mathbf{f}_1^* \mathbf{W}_f \mathbf{f}_2, \quad (2.5)$$

$$\langle \mathbf{q}_1, \mathbf{q}_2 \rangle_r = \mathbf{q}_1^* \mathbf{W}_r \mathbf{q}_2, \quad (2.6)$$

where \mathbf{W}_f and \mathbf{W}_r are positive-definite matrices that take into account the numerical discretization and the choice of norm for the forcing and the responses, respectively. The SVD is performed on $\mathbf{H}_W = \mathbf{W}_r^{1/2} \mathbf{H} \mathbf{W}_f^{-1/2}$ using the L_2 inner product, $\langle \mathbf{a}, \mathbf{b} \rangle = \mathbf{a}^* \mathbf{b}$, such that

$$\mathbf{H}_W = \sum_{j=1}^N \sigma_j \boldsymbol{\psi}_{W,j} \boldsymbol{\phi}_{W,j}^*. \quad (2.7)$$

The response and forcing modes of \mathbf{H} are then $\boldsymbol{\psi}_i = \mathbf{W}_r^{-1/2} \boldsymbol{\psi}_{W,i}$ and $\boldsymbol{\phi}_i = \mathbf{W}_f^{-1/2} \boldsymbol{\phi}_{W,i}$, respectively.

Following Fosas de Pando & Schmid (2017) and assuming that $\widehat{\mathbf{L}} = \widehat{\mathbf{L}}(\theta)$, $\mathbf{W}_r = \mathbf{W}_r(\theta)$, and $\mathbf{W}_f = \mathbf{W}_f(\theta)$, where θ is an arbitrary scalar parameter, the partial derivative of σ_i with respect to θ is

$$\frac{\partial \sigma_i}{\partial \theta} = -\sigma_i \Re(\langle \mathbf{H} \frac{\partial \widehat{\mathbf{L}}}{\partial \theta} \boldsymbol{\psi}_i, \mathbf{W}_r \boldsymbol{\psi}_i \rangle) + \frac{\sigma_i}{2} \langle \boldsymbol{\psi}_i, \frac{\partial \mathbf{W}_r}{\partial \theta} \boldsymbol{\psi}_i \rangle - \frac{\sigma_i}{2} \langle \boldsymbol{\phi}_i, \frac{\partial \mathbf{W}_f}{\partial \theta} \boldsymbol{\phi}_i \rangle. \quad (2.8)$$

The partial derivatives of the matrices can be computed either analytically if the mean flow field is independent of θ or by a finite-difference approximation. Note that computing $\partial \sigma_i / \partial \theta$ does not involve the calculation of \mathbf{H} or a separate SVD at $\theta + \Delta\theta$. It requires only the construction of the sparse matrices, $\widehat{\mathbf{L}}$, \mathbf{W}_r , and \mathbf{W}_f at θ and $\theta + \Delta\theta$, or their derivatives.

2.2. Adaptive resolvent analysis

We are interested in an efficient quantification of amplification, as characterized by the resolvent norm, σ_1 , in a range of spectral space. Adaptive resolvent analysis provides an alternative to a looping parameter sweep. We describe the procedure here under the parallel flow assumption for compressible boundary layers, such that the parameters of interest are the streamwise wavenumber, k_x , the spanwise wavenumber, k_z , and the wave speed $c = \omega/k_x$. Since the relevant wavenumbers and singular values can span several orders of magnitude, we consider the variation of the logarithm of the premultiplied linear amplification,

$$g = \log_{10}(\sigma_1^2 k_x k_z), \quad (2.9)$$

and its logarithmic derivatives,

$$g_j = \frac{\partial g}{\partial \log_{10}(k_j)} = \frac{2k_j}{\sigma_1} \frac{\partial \sigma_1}{\partial k_j} + 1, \quad (2.10)$$

where $j = x$ or z .

In practice, the scheme can be initiated with a coarse equidistant sampling of parameter space. Here, the scheme is initiated with only four samples in a region with small g to illustrate the performance of the scheme. At each iteration i , the samples (k_x^i, k_z^i) are used to measure g^i and its gradients (g_x^i, g_z^i) by computing Eqs. (2.9)-(2.10). After each iteration, the samples and measurements are used to construct an interpolant, m , between the samples and the measurements through GPR, which also computes the uncertainty, s , of the interpolant. The GPR algorithm used here is adapted from Eriksson *et al.* (2018), where the kernel functions are squared exponentials.

The next point to sample is the global maximum of an acquisition function $f_{ac}(m, s)$. Though there are several options for f_{ac} (Huhn & Magri 2022), we use

$$f_{ac}(m, s) = \kappa s + s^a(m - \min(m)). \quad (2.11)$$

The positive constants a and κ are used to tune the relative importance of exploration and exploitation. A larger value of κ increases exploration by increasing the weight on s , thus sampling regions with high uncertainty. The second term increases exploitation by looking for the largest values of the model, m . Since $s = 0$ for points that are already sampled and $f_{ac} > 0$, the global maxima of f_{ac} will always produce new points to sample.

Although a Matérn kernel could be used to capture sharper features (Huhn & Magri 2022), we used the squared exponential kernel, which limits m to smoother interpolants of g . For incompressible turbulent boundary layer flows, this is not an issue because $\omega \in \mathbb{R}$ and the spectrum of $\widehat{\mathbf{L}}$ is in the lower-half plane, so there is no discontinuity in σ_1 . For the case of compressible boundary layer flows, there exists a distinct region delineated by the relative Mach number,

$$\overline{Ma} = \frac{Ma(\overline{U} - c)k_x}{(k_x^2 + k_z^2)^{1/2}\overline{T}^{1/2}}, \quad (2.12)$$

where $\overline{Ma} \geq 1$ allows for the existence of freestream modes (Mack 1984; Bae *et al.* 2020). Due to the existence of these freestream modes, $\sigma_1(k_x, k_z, c)$ becomes discontinuous at $\overline{Ma} = 1$, the relative Mach line. In order to resolve this discontinuity, two separate GPRs are applied—one for $\overline{Ma} > 1$ and one for $\overline{Ma} < 1$. \overline{Ma} and its influence on freestream modes can be predicted *a priori* (Mack 1984); therefore, this delineation can be performed before computing the sweep.

In the case of flows where the spectrum has a discontinuity that is not known *a priori*, a different kernel function can be used for the GPR that accounts for discontinuities (Pang *et al.* 2019), though these kernels typically require the tuning of more hyperparameters. If the kernel functions are non-differentiable, the algorithm of Eriksson *et al.* (2018) cannot be used because it requires derivatives of the kernels. Using GPR with only measurements of g may require more samples in lieu of measurements of the gradients.

We apply the adaptive resolvent analysis to the following high-speed flows: a boundary layer over a flat plate followed by a compression ramp with either a CPG or a CIG, and a mixture of (ideal) gases in chemical non-equilibrium.

2.3. Calorically imperfect ideal gas

The full Navier-Stokes equations (NSE) with a CIG, after normalization by the freestream variables and the local boundary layer thickness, δ_{99} , are

$$\tilde{\rho} \frac{D\tilde{\mathbf{u}}}{Dt} = -\frac{1}{\gamma_\infty Ma^2} \nabla \tilde{p} + \frac{1}{Re} \nabla \cdot \tilde{\tau}, \quad (2.13)$$

$$\tilde{\rho} c_v \frac{D\tilde{T}}{Dt} = -(\gamma_\infty - 1) \tilde{p} \nabla \cdot \tilde{\mathbf{u}} + \gamma_\infty (\gamma_\infty - 1) \frac{Ma^2}{Re} \tilde{\tau} : \nabla \tilde{\mathbf{u}} + \frac{\gamma_\infty}{Pr Re} \nabla \cdot (\tilde{k} \nabla \tilde{T}), \quad (2.14)$$

$$\frac{D\tilde{p}}{Dt} = -\tilde{\rho} \nabla \cdot \tilde{\mathbf{u}}, \quad (2.15)$$

$$\tilde{p} = \tilde{\rho} \tilde{T}, \quad (2.16)$$

$$\tilde{\tau} = \tilde{\mu} \left(\nabla \tilde{\mathbf{u}} + \nabla \tilde{\mathbf{u}}^T - \frac{2}{3} (\nabla \cdot \tilde{\mathbf{u}}) \mathbf{I} \right). \quad (2.17)$$

The viscosity $\mu(T)$ is determined by Sutherland's law. For the CPG, the specific heat capacity at constant volume, c_v , is constant. For the CIG case, $c_v(T)$ is computed from McBride's (2002) polynomials.

The state, $\tilde{\mathbf{q}} = [\tilde{\mathbf{u}}, \tilde{T}, \tilde{\rho}]$, contains velocity, temperature, and density, respectively. The inner products are chosen to be equal so that $\mathbf{W} = \mathbf{W}_r = \mathbf{W}_f$ enforce the Chu (1965) norm along with the relevant numerical integration weights,

$$\mathbf{W} = \text{diag} \left(\bar{\rho}, \bar{\rho}, \bar{\rho}, \frac{\bar{c}_v \bar{\rho}}{Ma^2 \gamma_\infty (\gamma_\infty - 1) \bar{T}}, \frac{\bar{T}}{\gamma_\infty Ma^2 \bar{\rho}} \right). \quad (2.18)$$

We consider the case with $Re = \rho_\infty U_\infty \delta_{99} / \mu_\infty = 3 \times 10^4$, $Ma = U_\infty \sqrt{\rho_\infty} / \sqrt{p_\infty \gamma_\infty} = 5$, and $Pr = c_p \mu / k = 0.72$, where k is the thermal conductivity, c_p is the specific heat capacity at constant pressure, and $\gamma = c_p / c_v$. The freestream temperature, T_∞ , is 500 K with a cooled wall at 1600 K. Mean fields are obtained from direct numerical simulations of Di Renzo *et al.* (2022), upstream of the compression ramp. Under the parallel flow assumption, $\bar{\mathbf{q}}(y) = [\bar{U}(y), 0, 0, \bar{T}(y), \bar{\rho}(y)]$. The CPG and CIG results each use a $\bar{\mathbf{q}}$ computed with the CPG and CIG assumptions, respectively.

2.4. Mixture of ideal gases in chemical nonequilibrium

For this case, the fluid is assumed to be a mixture of ideal gases (N_2 , O_2 , NO , N , O) in chemical nonequilibrium and in thermal equilibrium. The equations are nondimensionalized with the same quantities as above, except that the diffusion coefficients at the freestream, $D_{i,\infty}$, are also used to nondimensionalize the equations. Equations (2.13) and (2.17) still hold, albeit with thermophysical properties that depend on the mixture. The temperature, continuity, and state equations are then

$$\tilde{\rho} \tilde{c}_v \frac{D\tilde{T}}{Dt} = -(\gamma_\infty - 1) \tilde{p} \nabla \cdot \tilde{\mathbf{u}} + \gamma_\infty (\gamma_\infty - 1) \frac{Ma^2}{Re} \tilde{\tau} : \nabla \tilde{\mathbf{u}} + \frac{\gamma_\infty}{Pr Re} \nabla \cdot (\tilde{k} \nabla \tilde{T}) + \sum_i^{N_s} \left[\frac{\bar{M}_\infty}{M_i} \frac{\gamma_\infty - 1}{Re} \tilde{T} \nabla \cdot (\tilde{\rho}_i \tilde{\mathbf{V}}_i) - \tilde{e}_i \tilde{w}_i - \frac{\gamma_\infty}{Re} \tilde{c}_{pi} \nabla \tilde{T} \cdot \tilde{\rho}_i \tilde{\mathbf{V}}_i \right], \quad (2.19)$$

$$\frac{D\tilde{\rho}_i}{Dt} = -\tilde{\rho}_i \nabla \cdot \tilde{\mathbf{u}} - \frac{1}{Re} \nabla \cdot (\tilde{\rho}_i \tilde{\mathbf{V}}_i) + \tilde{w}_i, \quad (2.20)$$

$$\tilde{p} = \tilde{T} \sum_{i=1}^{N_s} \frac{\bar{M}_\infty}{M_i} \tilde{\rho}_i, \quad (2.21)$$

where subscripts $i = 1, \dots, 5$ denote N_2 , O_2 , NO , N , and O , respectively. Note that Eq. (2.19) is expressed this way to ease comparison with Eq. (2.14) and to avoid time derivatives of p present when considering enthalpy transport. The diffusive flux is defined as

$$\tilde{\rho}_i \tilde{\mathbf{V}}_i = -\frac{\tilde{D}_i}{Sc_i} \frac{\tilde{\rho}_k M_i}{M_k} \nabla \tilde{X}_i + \tilde{Y}_i \sum_{j=1}^{N_s} \frac{\tilde{D}_j}{Sc_j} \frac{\tilde{\rho}_k M_j}{M_k} \nabla \tilde{X}_j, \quad (2.22)$$

where $\tilde{Y}_i = \tilde{\rho}_i / \tilde{\rho}$ and $\tilde{X}_i = \tilde{\rho}_i M_k / (\tilde{\rho}_k M_i)$ are the mass fraction and mole fraction of species i , respectively. Details of the transport and thermal coefficients are reported by Di Renzo *et al.* (2020).

The state is $\tilde{\mathbf{q}} = [\tilde{\mathbf{u}}, \tilde{T}, \tilde{\rho}_1, \dots, \tilde{\rho}_5]$, where $\mathbf{W}_r = \mathbf{W}_f = \mathbf{W}$ is defined as

$$\mathbf{W} = \text{diag} \left(\bar{\rho}, \bar{\rho}, \bar{\rho}, \frac{\bar{\rho} \bar{c}_v}{\bar{T} Ma^2 \gamma_\infty (\gamma_\infty - 1)}, \frac{\bar{M}_\infty \bar{T}}{M_1 \gamma_\infty Ma^2 \bar{\rho}_1}, \dots, \frac{\bar{M}_\infty \bar{T}}{M_5 \gamma_\infty Ma^2 \bar{\rho}_5} \right). \quad (2.23)$$

There is a discrepancy with the Chu norm used by Franko *et al.* (2010) and Eq. (2.23) due to the treatment of the $\bar{\rho}_i^{-1}$ terms. Here, regularization is applied by using $(\bar{\rho}_i + \epsilon)^{-1}$, with $\epsilon \ll 1$, instead of $\bar{\rho}_i^{-1}$ to avoid division by zero in the freestream where the densities of NO, N, and O vanish. Finally, this norm also removes the influence of $p\nabla \cdot \mathbf{u}$ terms so that Eqs. (2.23) and (2.18) are analogous.

Two separate mean flows are studied, both with $Re = 7.3 \times 10^4$, $Ma = 10.2$, and $Pr = 0.71$, with a freestream temperature of $T_\infty = 1040$ K and a cooled wall at 1700 K. One is a similarity solution of a mixture of ideal gases, as described by Di Renzo & Urzay (2021). The second is a similarity solution of a CPG. The $\tilde{\mu}(\tilde{T})$ values differ between the two flows, as the latter uses a power law and the former is based on the thermochemical state of the mixture.

2.5. Numerical analysis

The relevant equations for each case are discretized using summation by parts (SBP) with a rational transformation that clusters half the points in y between 0 and 1 and the other half between 1 to 5. Isothermal and no-slip boundary conditions are applied at the wall. For the chemically reacting flow, the wall-normal diffusive velocities, V_i , are set to 0 at the wall. In the freestream, a damping layer and artificial viscosity are applied at the last 5% of the domain to absorb any reflections, as done by Madhusudanan & McKeon (2022). Finally, filtering is applied to the resolvent operator to smooth out sawtooth oscillations by using the filter described by Lele (1992).

Due to the SBP scheme, the ensuing discretizations of $\hat{\mathbf{L}}$ are sparse and banded. In the calculations, the matrix inverse is never explicitly computed; instead, a lower-upper (LU) decomposition of $(-i\omega\mathbf{I} + \hat{\mathbf{L}})$ is used. An Arnoldi algorithm then computes the SVD of \mathbf{H}_W , where the product $\mathbf{x} = \mathbf{H}\mathbf{b}$ is computed as the solution to $(-i\omega\mathbf{I} + \hat{\mathbf{L}})\mathbf{x} = \mathbf{b}$ through the LU decomposition. The Arnoldi algorithm uses at most 300 iterations and stops if σ_{10} has converged to within 10^{-6} .

3. Results

To demonstrate the effectiveness of the adaptive resolvent scheme, we apply it over $k_x = 2\pi/\lambda_x$ and $k_z = 2\pi/\lambda_z$ at fixed $c = \bar{U}(y^+ \approx 15)$ to the resolvent analysis of the CPG and the CIG flows in Figure 1(a) and 1(b), respectively. The contours are computed using an equidistant (in log-space) grid with 72 points in λ_x and 70 points in λ_z along with their sampled points in black circles and the initially sampled points as white triangles. Despite being initialized in a region with small g , the adaptive resolvent analysis is able to identify and cluster samples in the regions in spectral space with large g . Because the scheme is applied independently in the two regions across the relative Mach line, each individual scheme operates with no knowledge of the global maxima or the other region. For reference, the interpolant m computed from the samples shown in Figure 1(b), is included in Figure 1(c) to illustrate that the GPR can create an approximate model of g , even in regions with sparse measurements. Because the kernel functions are squared exponentials, sharper features in the relatively supersonic region are smeared out in m when compared with g .

Between the CPG and CIG assumptions, $\bar{\gamma}$ differs the most where the temperature is highest. For boundary layer flows, this occurs near the wall, within the boundary layer, as shown in Figure 1(g). The modes within the relatively subsonic region, which have support only within the boundary layer, exhibit the largest sensitivity to changes

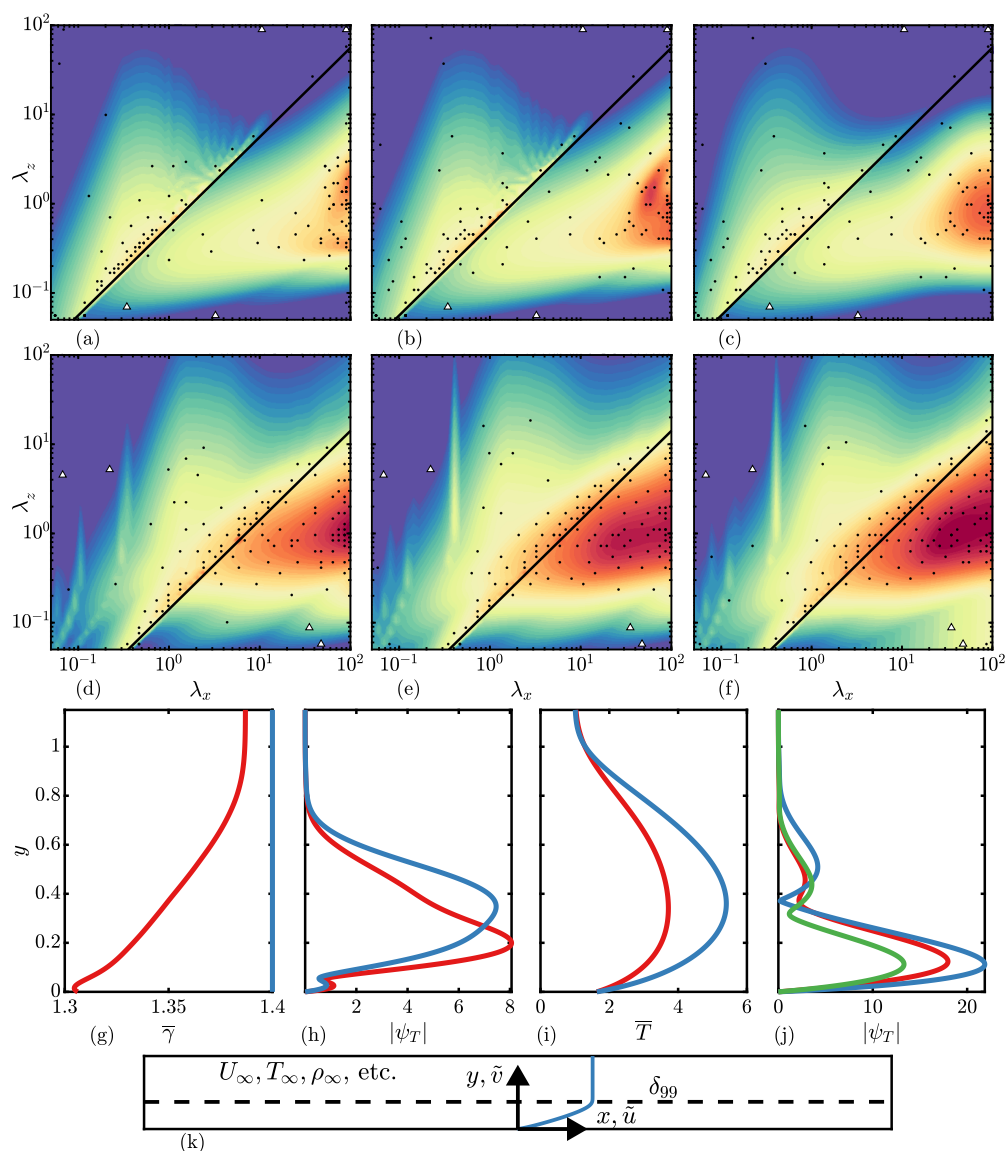


FIGURE 1. Contours of g computed from the CPG (a) and CIG (b) flows described in Section 2.3 with $c = \bar{u}(y^+ \approx 15)$ and the interpolant m (c) computed from the samples of g of the latter flow using GPR. Contours of g computed from the CPG flow described in Section 2.4, the chemically reacting base flow (d), with the linearized dynamics under a frozen chemistry assumption (e), and the chemically reacting base flow with a chemically reacting linearized base flow (f) using $c = \bar{u}(y^* \approx 18)$. In (a-f), the black solid line denotes a relative Mach number of one. The contours are logarithmically spaced from 500 in blue to 1.25×10^7 in red. In (a,b,d,e,f), the black circles denote the points sampled, whereas the white triangles denote the initial sample points. (g) shows $\bar{\gamma}$ and (h) shows the temperature component of the response mode computed at $\lambda_x = 60$, and $\lambda_z = 1$ for the CPG (blue) and CIG (red) flows. (i) shows the \bar{T} from the base flow from (d) in blue and (e,f) in red. The temperature component of representative modes from (d) in blue, (e) in green, and (f) in red are shown in (j) for $\lambda_x = 60$ and $\lambda_z = 1$. Schematic of the flow field, geometry, and coordinate axes with dashed line denoting δ_{99} and \bar{u} in the blue line (k).

in $\bar{\gamma}$. The relatively supersonic region has modes with support in the freestream, where the temperatures and $\bar{\gamma}$ are constant and exhibit less sensitivity to changes in the CPG assumption. The most appreciable differences in the contours of Figures 1(a,b) occur in the relatively subsonic region, primarily in regions with largest λ_x . Representative temperature components of the response modes plotted in Figure 1(h) have significant structural differences, notably a difference in the location of peak amplitude.

The adaptive scheme is applied to the hypersonic similarity solution base flows with the CPG ideal gas in Figure 1(d) and the mixture of ideal gases in chemical nonequilibrium and thermal equilibrium in Figure 1(f) with $c = \bar{u}(y^* \approx 19)$. Because the $1/Ma^2$ coefficients in the inner products in Eqs. (2.18) and (2.23) decrease with increasing Ma , the discontinuity between the relatively subsonic and relatively supersonic regions is less apparent for the hypersonic flow than the supersonic flows in Figures 1(a,b). The supersonic modes are still present above the relative Mach line with support in the freestream. The freestream modes are pressure modes (Mack 1984); thus, the T and ρ (ρ_i for the mixture) components of ψ_i and ϕ_i have non-negligible freestream support. The inner product adds a $1/Ma^2$ bias to the T and ρ components of the modes. As a result, the contribution to the linear amplification, σ_1 , is primarily from the hydrodynamic components of the flow.

The differences between the amplification in chemical nonequilibrium and the CPG are once again primarily in the relatively subsonic region, where the modes have support within the boundary layer and where the chemical production and diffusive terms are largest due to the elevated temperatures, plotted in Figure 1(i). As a result, there are non-negligible concentrations of NO, N, and O within the boundary layer, particularly close to the wall (Di Renzo & Urzay 2021), which cause significant differences in the chemical, thermal, and momentum transport coefficients. In the relatively supersonic region, the freestream modes are qualitatively similar because they experience constant freestream conditions with lower temperatures that reduce the chemical production and diffusive terms.

The base flows used in Figure 1(d,f) differ because the thermophysical properties are computed using different models, and as a result, the \bar{T} profiles are quantitatively different. To isolate the effect of the chemical nonequilibrium terms in the linearized NSE from the changes in the base flows, the calculations are repeated in Figure 1(e) with the equations linearized about the same chemically reacting base flow as in Figure 1(f) with the flow treated as a single-species CIG. The transport coefficients are computed from the same chemistry model as the flow in chemical nonequilibrium and are then assumed to vary only with temperature when constructing the linearized NSE.

The differences between Figure 1(e) and 1(f) are once again in the region with large λ_x and $\lambda_z \sim \mathcal{O}(1)$, where the flow in chemical nonequilibrium has larger amplification. In nonnormal operators such as $\hat{\mathbf{L}}$, the resolvent norm, σ_1 , increases when there are more sources of shear. The chemical production terms add sources of shear to $\hat{\mathbf{L}}$ present within the boundary layer where \bar{T} is largest, thus increasing σ_1 . As a result, the differences in amplification are present in the relatively subsonic region, where the modes have support only in the boundary layer. We note that there is a difference in amplification in the lower right-hand corner of Figure 1(f), where $\lambda_z \ll \lambda_x$ in the limit of extremely long and thin structures that are not expected to be present in physical flows. Due to the increase in the viscous terms ($\sim Re^{-1}\rho^{-1}\mu k_z^2$) in this region of spectral space, the modes experience damping that forces them away from the boundary layer, making these modes unphysical, and is a consequence of the small Re used here.

Representative modes for Figure 1(d,e,f) are plotted in Figure 1(j), with red denoting

the CPG flow, green the CIG flow using the chemically reacting base flow, and blue the results with chemical nonequilibrium. All modes are centered at the critical layer location, indicating that this is still a source of amplification for these modes. However, the relative amplitudes of the modes differ, even when the same base flow is used. This illustrates that the chemical production terms can impart structural differences in the modes, as well as their linear amplification. Of further interest is the use of masking of the resolvent operator to query the amplification mechanisms between different state variables or regions in physical space, similar to the approach employed by Magri *et al.* (2017) for eigenvalue sensitivity.

4. Conclusions

A scheme is presented to efficiently and adaptively sample the regions in the parameter space where the amplification is the largest, using local measurements at the sampled points. This method is based on Bayesian optimization by creating an acquisition function $f_{ac} = f_{ac}(m, s)$ through GPR. As a proof of concept, the method is shown to identify the regions in spectral space with the largest linear amplification for a CPG, a CIG, and a mixture of ideal gases in chemical nonequilibrium under the parallel flow assumption.

Because of the large temperatures within the boundary layer, the temperature-dependent thermophysical properties are expected to vary most within the boundary layer and, in the case of flow in chemical nonequilibrium, lead to the production of NO, N, and O. As a result, the differences in spectral space are most pronounced in the relatively subsonic region, where the resolvent modes are expected to have support only within the boundary layer. The modes in the relatively supersonic region have support within the boundary layer, but the mechanism that leads to their amplification is an inviscid phenomenon in the freestream region. The differences in amplification when chemistry is incorporated or when the CPG assumption is relaxed to a CIG assumption in spectral space are localized in the region with the largest λ_x and $\lambda_z \approx \lambda_x/10$.

Chemical nonequilibrium terms can increase the linear amplification of the linearized NSE by providing more shear terms. These terms also create quantitative differences in the response modes, which can indicate differences in flow structures from control inputs. Since these terms are computed from a specific chemistry model, this linear analysis can be used to predict which length and timescales are most sensitive to the choice of chemistry model. Further work will incorporate turbulent, chemically reacting mean flows to understand how scale separation affects the results described herein and also consider the nonparallel streamwise development of real boundary layer flows.

Acknowledgments

The authors acknowledge use of computational resources from the Yellowstone cluster awarded by the National Science Foundation to CTR.

REFERENCES

- BAE, H. J., DAWSON, S. T. & MCKEON, B. J. 2020 Resolvent-based study of compressibility effects on supersonic turbulent boundary layers. *J. Fluid Mech.* **883**, A29.
- CHU, B.-T. 1965 On the energy transfer to small disturbances in fluid flow (part I). *Acta Mech.* **1**, 215–234.
- DI RENZO, M., FU, L. & URZAY, J. 2020 HTR solver: an open-source exascale-oriented

- task-based multi-GPU high-order code for hypersonic aerothermodynamics. *Comput. Phys. Commun.* **255**, 107262.
- DI RENZO, M. & URZAY, J. 2021 Direct numerical simulation of a hypersonic transitional boundary layer at suborbital enthalpies. *J. Fluid Mech.* **912**.
- DI RENZO, M., WILLIAMS, C. T., URZAY, J. & PIROZZOLI, S. 2022 Stagnation enthalpy effects on turbulent Mach 5 compression corner flow. *Proceedings of the CTR Summer Program*, Center for Turbulence Research, Stanford University, pp.xx–xx .
- ERIKSSON, D., DONG, K., LEE, E., BINDEL, D. & WILSON, A. G. 2018 Scaling Gaussian process regression with derivatives. *Adv. Neur. In.* **31**.
- FOSAS DE PANDO, M. & SCHMID, P. J. 2017 Optimal frequency-response sensitivity of compressible flow over roughness elements. *J. Turbul.* **18**, 338–351.
- FRANKO, K., MACCORMACK, R. & LELE, S. 2010 Effects of chemistry modeling on hypersonic boundary layer linear stability prediction. *AIAA Paper 2010-4601*.
- HUHN, F. & MAGRI, L. 2022 Gradient-free optimization of chaotic acoustics with reservoir computing. *Phys. Rev. Fluids* **7**, 01442.
- LELE, S. K. 1992 Compact finite difference schemes with spectral-like resolution. *J. of Comput. Phys.* **103**, 16–42.
- MACK, L. M. 1984 Boundary-layer linear stability theory. *Tech. Rep.*, Jet Propulsion Lab, California Institute of Technology.
- MADHUSUDANAN, A. & MCKEON, B. J. 2022 Subsonic and supersonic mechanisms in compressible turbulent boundary layers: a perspective from resolvent analysis. arXiv:2209.14223 [physics.flu-dyn]. .
- MAGRI, L., SEE, Y.-C., TAMMISOLA, O., IHME, M. & JUNIPER, M. 2017 Multiple-scale thermo-acoustic stability analysis of a coaxial jet combustor. *P. Combust. Inst.* **36**, 3863–3871.
- MCBRIDE, B. J. 2002 NASA Glenn coefficients for calculating thermodynamic properties of individual species. *Tech. Pub.*, John H. Glenn Research Center, National Aeronautics and Space Administration.
- MOARREF, R., SHARMA, A. S., TROPP, J. A. & MCKEON, B. J. 2013 Model-based scaling of the streamwise energy density in high-Reynolds-number turbulent channels. *J. Fluid Mech.* **734**, 275–316.
- PANG, G., YANG, L. & KARNIADAKIS, G. E. 2019 Neural-net-induced Gaussian process regression for function approximation and PDE solution. *J. Computat Phys.* **384**, 270–288.